

Spectroscopic Characterization of Er,Yb:Y₂Ti₂O₇ Phosphor for Latent Fingerprint Detection

Mouna Gouiaa^a, Ines Bennour^a, Lamia Rzouga^b, Alessandra Toncelli^{c*}, Jihua Xu^c, Aïcha Mbarek^e, Aldo Moscardini^d, Najoua Essoukri^b and Ramzi Maalej^a

^a Laboratoire Géorressources, Matériaux, Environnement et Changements Globaux, Faculty of Sciences of Sfax, Sfax University, 3018 Sfax, Tunisia

^b Université de Sousse, Ecole Nationale d'Ingénieurs de Sousse, LATIS-Laboratory of Advanced Technology and Intelligent Systems, 4023, Sousse, Tunisia

^c Istituto Nanoscienze CNR Italy and Dipartimento di Fisica "Enrico Fermi", University of Pisa, Largo B. Pontecorvo, 3, 56127 Pisa, Italy

^d NEST, Scuola Normale Superiore Piazza San Silvestro 12 56127 Pisa

^e Laboratory of Advanced Materials, National Engineering School, University of Sfax, BP 1173-3038 Sfax-Tunisia.

* Corresponding author: E-mail: alessandra.toncelli@unipi.it

Keywords: Nanoparticles, rare earth, luminescence, latent fingerprint, Erbium, Ytterbium, minutiae extraction, fingerprint quality

Abstract

Er³⁺ doped and Er³⁺/Yb³⁺ co-doped Y₂Ti₂O₇ phosphors with various concentrations of Er³⁺ (12-20%), Yb³⁺ (1-10at%), and Er³⁺Yb³⁺ (1%, and 1,2,3%, respectively) were prepared by solid-state reaction. The phase structure, and purity of all prepared phosphors, were studied by X-ray diffraction analysis followed by measurement of the hydrodynamic diameter of each sample by Dynamic light scattering. The formation of the pyrochlore structure was confirmed by the observation of relative vibrations by Fourier Transform Infrared Spectroscopy. Moreover, photoluminescence spectra of different co-doped Y₂Ti₂O₇ compounds are presented in order to check the energy transfer processes of Er³⁺ and Yb³⁺ ions. Finally, phosphors were used for the detection of latent fingerprints on various surfaces and a fingerprint minutia extraction algorithm was used for the analysis of extracted minutiae. The analyses confirm that the co-doped phosphors can be useful for the visualization of latent fingerprints once a good detection of their minutiae is obtained.

1. Introduction

In forensic science, the fingerprint identification technology is an established technique thanks to the fact that fingerprints are unique for each person and finger and that they do not vary with age.

Perspiration continuously produces sebum and sweat which can leave traces when a finger touches different surfaces [1-4]. Thanks to this, the extraction of latent fingerprints is one of the first actions to take in a crime scene. Unfortunately, the collection of these traces can be difficult in some cases due to the nature of the touched surface especially if fingers were not tainted with colored products such as blood [5,6]. Moreover, the fingerprints left on smooth surfaces are particularly hard to find. In most cases, only level 1 and level 2 ridge details are observed, however, few groups have succeeded to visualize even level 3 ridge details (sweat pores) [7-11].

For these reasons, it is important to increase the efficiency of the powder dusting method, which is the easiest and most widely used method for fingerprint visualization as compared to other techniques such as ninhydrin fuming, silver nitrate spraying, etc [11,12]. One of the main advantages of this method is that the whole process can last only 30 seconds if put into practice by expert investigators [9]. Unfortunately, commercial magnetic powders usually used for this purpose have shortcomings concerning their high background interference, low contrast and sensitivity [13-15]. Research on the optimization of new materials that can be useful alternatives to commercial products is very lively. In particular, fluorescent materials can allow a better visualization of latent fingerprints with lower background interference and higher sensitivity. A good material for fingerprint detection should have uniform morphology, strong emission, good stability, and an inert nature against the humid environment. Besides, the size of powder grains can play a role: nano-sized powders usually show better adhesion if compared to larger ones [16-19], but nano-sized objects are generally highly reactive and, since they can enter the body through inhalation or skin contact, they also deserve consideration about personal and environmental safety.

Lanthanide ions are usually considered biocompatible materials, especially Er^{3+} , Eu^{3+} , Gd^{3+} , Sm^{3+} , Yb^{3+} and Y^{3+} ions which are found to have a relatively low toxicity [20-23]. Many works focus on rare earth ion doped luminescence materials because of the peculiar optical properties arising from the intra 4f transitions. In fact, the emission bandwidth of a rare earth ion is much sharper than the emission bandwidth of metals or semiconductor materials. Moreover, lifetimes are several orders of magnitudes longer and they have already shown to be useful for this purpose [22]. As a result, fluorescent powders based on rare-earth doped materials can allow the detection of latent finger-marks on a broad range of surfaces, such as porous, semi-porous, non-porous and even aged finger-marks [24]. For these reasons, active research is being carried out to develop more efficient stable and reliable rare-earth phosphors [25,26]. Indeed, no universally recognized conclusions have been drawn on what material is the best to be used for this application, yet. Recently, some works focused on the upconversion emission properties of the rare earth ions because this could allow latent fingermarks visualization with good contrast and without background interference [24,27,28], including the lighting source. In this respect, fluorides are usually considered very good upconverting materials, although they are usually difficult to grow with high quality. On the other hand, oxide materials usually show lower upconversion efficiency, but they can give rise to strong Stokes emission and are in general easier to grow than fluoride materials. Moreover, the upconversion efficiency is generally low, with quantum yield in the few % range [29], therefore, the Stokes emission can provide much better visualization efficiency provided that the Stokes shift is high enough to avoid interference. In particular, UV illumination does not provide visual interference between the illumination source and the fluorescence. $\text{Y}_2\text{Ti}_2\text{O}_7$ belongs to the pyrochlore class and possesses peculiar thermodynamic and dynamic magnetic properties at low temperatures [30]. This powder caught the attention of researchers because of its Stokes and upconversion emission [31-37] when doped with other rare earth ions or for ion-detection [38]. Moreover, it possesses relatively low phonon energy ($\omega \approx 712\text{cm}^{-1}$) that can result in low non radiative energy losses, it is chemically stable and can be easily grown in powder form. In this work, we report the successful preparation of novel and non-toxic powder based on highly

luminescent Er^{3+} and $\text{Er}^{3+}/\text{Yb}^{3+}$ codoped $\text{Y}_2\text{Ti}_2\text{O}_7$ phosphors for fingerprint detection through solid-state method. To this aim, crystal structure and luminescence properties have been studied as a function of the concentration of Er^{3+} ions. Moreover, we use the optimized co-doped $\text{Y}_2\text{Ti}_2\text{O}_7$ phosphors to detect fingerprints on the surface of different objects among which we choose several items commonly employed in daily life, such as glass, Compact Disc (CD), aluminium foil and plastic, where fingerprints are often left. Finally, a fingerprint minutiae detection algorithm is applied to analyze the quality of extracted minutiae in order to demonstrate the competitive performances.

2. Materials and Methods

2.1. Preparation of samples

$\text{Y}_{1-x}\text{Er}_x\text{Ti}_2\text{O}_7$ (Er:YTO) ($x=12,14,16,18,20$ at%), $\text{Y}_{1-y}\text{Yb}_y\text{Ti}_2\text{O}_7$ (Yb:YTO) ($y=1,5,10$ at%), and $(\text{Y}_{1-(x+y)}\text{Er}_x\text{Yb}_y\text{Ti}_2\text{O}_7)_2$ ($x = 1$ at% and $y = 1,2,3$ at%) (Er,Yb:YTO) phosphors were synthesized via the solid state method. Four different oxides (Y_2O_3 (99.99%), TiO_2 (99.9%), Yb_2O_3 (99.98%) and Er_2O_3 (99.9%)) (Alfa Aesar) were used for the preparation of the various compositions. The starting materials were prepared by grinding the corresponding stoichiometric composition with some drops of acetone in a ball mill agate mortar for three hours, until they were ground homogeneously. The materials were pre-sintered under air atmosphere at 800°C for 4 h, and then sintered at 1200°C for 5 h. The mixture was pelletized and heated repeatedly at 1500°C for 5h. Pellets of 10 mm in diameter and 2 mm in thickness were prepared.

2.2. Experimental techniques

The phase structure of samples was analyzed by X-ray diffraction (XRD) pattern with a Panalytical X' Pert diffractometer using CuK α radiation (1.5404 \AA) at 30 kV and 15 mA in the range 10° - 70° with a step size of $2\theta = 0.02$. The crystallographic phases were identified by comparison with the X-ray patterns of the JCPDS database. The crystallographic parameters were refined using the Rietveld-fit program [39].

The particle size of the powders (hydrodynamic diameter) was determined with a Zeta Sizer Nano ZS (Malvern Instruments Inc., UK) using the technique of dynamic light scattering. The measurements were performed in a polypropylene cuvette at room temperature. The average hydrodynamic diameter was calculated from the autocorrelation function of the intensity of scattered light from the nanoparticles by DTS Nano software. The samples (solid status) were dispersed in deionized water and sonicated to separate aggregates of nanoparticles (NPs), just before the measurement.

Fourier-transform infrared (FTIR) spectrum of the samples was recorded using Nicolet 5SX-FTIR spectrometer equipped with a diamond micro-ATR accessory and working with OMNIC software. Spectra were recorded from 800 to 400 cm^{-1} at a spectral resolution of 4 cm^{-1} and 32 scans were accumulated for improving the signal/noise ratio.

Photoluminescence (PL) measurements were performed by exciting the samples with a visible laser line at 448 nm . The PL emission was collected and fiber-coupled to a compact spectrometer equipped with a linear array of detectors (Ocean Optics HR4000).

2.3. Latent fingerprint minutia extraction

Biometric systems relying on fingerprint mostly use the information of minutiae points for person authentication. Minutiae are very reliable with discriminative characteristics in fingerprints. They are classified according to four types: termination, bifurcation, island and lake. The most used minutiae are bifurcations and endings [40]. The accuracy of fingerprint matching techniques depends on the image quality [41].

To prove that the prepared Er,Yb:YTO phosphor presents satisfying performances as a fingerprint labelling agent, we opted for the fingerprint minutiae extraction algorithm to evaluate the visualization and the number of the fingerprints minutiae. The retained algorithm was developed in [42] based on preprocessing and minutiae extraction as follows:

- Preprocessing: It consisted in image enhancement to improve the image quality for better feature extraction following five main steps. It is ensured firstly by image normalization, secondly by the orientation of the peaks of the fingerprint, and thirdly by frequency estimation. Next, a segmentation step of the region of interest is applied to identify the peak regions of a fingerprint image, to construct a mask so as to identify that region, and to normalize image intensity values. Finally, we apply oriented Gabor filters.
- Feature extraction: The minutiae feature extraction step is applied on the enhanced gray-scale image. After image binarization, we apply a morphological thinning operation, where ridge structures are reduced to pixel thickness, referred to as the skeleton. We analyze the obtained thinned binary image in each pixel 'p' to find minutiae location by having the 8-neighbourhood (pixels within 3×3 window centred at p) circularly traversed in an anti-clockwise way to yield the Rutovitz crossing number [43] (Equation 1):

$$cn(p) = \frac{1}{2} \sum_{i=1..8} val(p_{(i \bmod 8)}) - val(p_{i-1}) \quad (1)$$

where $val \in \{0,1\}$

Then we identify minutiae pixel locations, as ridge endings will have cn equal to 1 and ridge bifurcations will have cn equal to 3.

3. Results and discussion

3.1. XRD

Figure 1 shows the X-ray diffraction (XRD) patterns of Er:YTO, Yb:YTO and Er,Yb:YTO powders. All the peak patterns match well with that of YTO which is a single pyrochlore phase with cubic crystal structure and $Fd3m$ space group: (111), (311) and (331) diffraction peaks are pyrochlore lattice reflections, while (222), (400) and (622) are fundamental fluorite reflections. These results show that samples annealed at 1500°C are well crystallized and exhibit a pyrochlore superlattice structure according to the JCPDS N°42- 0413. Therefore, doping with Erbium and Ytterbium oxide using solid-state reaction synthesis does not have a significant influence on the pyrochlore phase. Indeed, the position of diffraction peaks at various doping levels does not change, and this means that the interfusion of the Erbium and Ytterbium ions were made successfully in substitution of Yttrium, which has a similar ionic radius. These results indicate that the high temperature with long reaction time sintering represents a cheap and effective method to achieve excellent pyrochlore oxides.

3.2. DLS measurements

Table 1 shows the hydrodynamic diameters obtained from the experimental measurements for each sample analyzed. The range of analyzed diameters goes from 325 nm of YTO: 1% Er/ 2% Yb up to 670 nm of YTO: 1% Er/ 1% Yb, while the polydispersity index (PDI) varies between 0.4 and 1.0. For NPs doped with Ytterbium the smallest size corresponds to 5% of Yb^{3+} (mean diameter 383 nm). For NPs doped with both Ytterbium and Erbium, the smallest size corresponds to 1% Er^{3+} and 2% Yb^{3+} . We observed that the variation of Yb^{3+} concentration (both reducing or increasing) leads to an increase in the hydrodynamic diameter. For NPs doped with Er^{3+} we did not observe a direct correlation between the size and the concentration of doping agent. The range of mean diameters is between 460 and 550 nm, with the only exception of NPs doped with 12% of Er^{3+} that showed a slightly larger dimension (637 nm).

3.3. FTIR spectroscopy

The infrared spectra of all prepared samples are present in Figure 2. This technique is effective to check the presence of the different elements by studying the obtained vibrational modes. The bands around 560, 460 and 410 cm^{-1} are assigned to Ti-O, Y-O and Y-O' stretching vibration in the $\text{Y}_2\text{Ti}_2(\text{O})_6\text{O}(2)$ polyhedron of YTO, respectively [35] which are the main features of titanate pyrochlore spectra. The presence of these vibration lines confirms the formation of the YTO phase with no detectable alterations. No other absorption bands from unwanted impurities were observed.

3.4. Spectroscopic investigation

A direct excitation of the Er^{3+} ions below the YTO band gap from the ground $^4\text{I}_{15/2}$ to the $^4\text{F}_{7/2}$ or $^2\text{H}_{11/2}$ levels yields a luminescence spectrum dominated by emission in the visible range extending mainly from 500–1000 nm. Figures 3 a) and b) show an overview of the room temperature emission spectra of Er:YTO under excitation at 448 nm after normalization to the 570 nm emission peak. According to the Dieke diagram, this pump radiation is absorbed by the $^4\text{F}_{5/2}$ Er^{3+} multiplet located at around 22000–22500 cm^{-1} . From this level, the energy is transferred to the closely spaced lower lying Er^{3+} levels and strong visible emission is usually obtained from $^4\text{S}_{3/2}$ and $^4\text{F}_{9/2}$ Er^{3+} multiplets.

UV irradiation like the one used for LFP visualization is expected to follow a similar path. As expected, under 448 nm pumping we obtained visible emission spectra composed of a few bands superimposed to a spurious broadband signal due to residual emission from the filter used to cut the laser stray light. All the narrow bands are characteristic of intra-4f-shell transitions of Er^{3+} ions [40] and can be easily assigned on the basis of the Dieke diagram. The two main bands lay in the green and red regions, that is, in the 550–600 nm and 650–700 nm ranges. Emission in the green region is due to two different overlapping transitions, namely $^4\text{S}_{3/2} \rightarrow ^4\text{I}_{15/2}$ and $^2\text{H}_{11/2} \rightarrow ^4\text{I}_{15/2}$. These two bands can be easily distinguished by the different intensity behavior as a function of the doping level. In fact, after normalizing the spectra to the strongest emission line of the $^4\text{S}_{3/2} \rightarrow ^4\text{I}_{15/2}$ transition (570 nm) the emission intensity of the other bands remain more or less constant. The weaker emission at around 658 nm is assigned to the $^4\text{F}_{9/2} \rightarrow ^4\text{I}_{15/2}$ transition. The weakest emission is located at 950–1000 nm and is assigned to the $^4\text{I}_{11/2} \rightarrow ^4\text{I}_{15/2}$ transition. This means that the population of the $^4\text{F}_{9/2}$ and $^4\text{I}_{11/2}$ levels scale very much like that of $^4\text{S}_{3/2}$, while that of $^2\text{H}_{11/2}$ does not. This permitted us to clearly identify the peaks that belong to $^2\text{H}_{11/2}$ even if its emission band overlaps that of $^4\text{S}_{3/2}$. The lack of any concentration quenching effect demonstrates the possibility to use high dopant concentration to enhance the emission intensity of the material, as already observed by Yin et al. for the upconverted emission [34].

In order to investigate the influence of a sensitizer, Yb^{3+} was added as a co-dopant. Emission spectra of 1%Er, x%Yb:YTO (x=1,3 at%) are displayed in figure 3b under 448 nm excitation after normalization to the green Er emission. The emission from 14%Er has been rescaled and added for comparison and easy identification of the emission bands. With these compositions, the strongest Er emission band in the green region is still evident and shows the same shape of the singly-doped

samples. Moreover, a strong emission band comprised of three peaks appear in the 950-1000 nm region. The shape and intensity of this band is very different from that of the singly Er-doped samples, therefore it is attributed to the $^2F_{5/2} \rightarrow ^2F_{7/2}$ Yb transition. The intensity of this band increases with Yb doping, as expected. No evidence of the $^4F_{9/2} \rightarrow ^4I_{15/2}$ Er transition is present in the 650-700 nm range. These results demonstrate the presence of a strong energy transfer process from Er to Yb, which could be responsible for the disappearing of the red Er emission band. Therefore, this composition allows to obtain a purely-green visible emission that could be interesting for fingerprint visualization as the green region is of maximum efficiency for the human eye.

3.5. Latent finger print detection using powder-dusting method

Based on the photoluminescence section, good visualization of the latent fingerprints (LFs) on different surfaces is expected. Wherefore, porous and non-porous surfaces (glass, plastic, aluminum foil, and compact disc) are selected to test our new powders. Before impression, the hand of fingerprint donor was washed and dried carefully. At that moment, the cleaned fingers wiped the foreheads of the fingerprint donor and pressed gently on several different surfaces at room temperature. Afterwards, Er,Yb co- doped YTO were stained on the LFPs by using soft feature brush with smooth brushing method. Finally, fresh fingerprints were formed and were ready to be visualized. The main goal of this experience is the production of fluorescent powder to make the latent fingerprints visible under UV irradiation. The schematic view for the fingerprints development is shown in Figure 4. Figures 5 a-h), show the fresh fingerprint images developed by Er,Yb:YTO phosphors respectively from aluminum foil, CD, plastic and glass. It can be noted that they show good adhesion to the finger mark ridges thanks to the characteristic small size of the nano-phosphors. In fact, fingerprint details are already clear even under visible illumination. Moreover, under UV illumination at 365 nm the finer details of fingermarks are even better visualized thanks to the bright green color shown by the powders in these conditions. These results prove that despite the large size of the grains, this new synthetic phosphor sample is producing satisfactory intense fingermark images since the different ridges were clearly observed.

Figure 6 shows a comparison of enlarged fingerprint pictures developed on aluminum foil under visible and UV light. The figure clearly shows that all the three levels of fingerprint ridge patterns are visualized: whorls (Level 1); ridge ends, islands, enclosures (Level 2), sweat pores and scars (Level 3).

3.6. Fingerprint minutia extraction

The proposed fingerprint minutia extraction algorithm was already evaluated and validated using the three public fingerprint databases: BioSecure, FVC DB1 and PolyU [41-44]. In those studies, high performances were achieved. Actually, the algorithm application for latent fingermarks stained by 1% Er, 3% Yb: YTO, respectively from an aluminum foil and a CD, shows promising initial results. Figure 7 illustrates the extracted minutiae on the example of two latent fingerprint images with an aluminum foil under UV illumination and a CD under UV illumination, which ensures good matching accuracy. As depicted in this figure, the number of extracted minutiae of the latent fingerprint varies with the surface on which the fingerprint is left. The analysis of the considered images highlights that the resulted latent fingerprints with an aluminum foil under UV illumination present a better quality with 292 minutiae compared to the resulted one with a CD under UV illumination with 685 minutiae. In fact, it is demonstrated that a high number of minutiae is due to false minutia caused by environmental conditions such as temperature, humidity and pressure. In such an issue, it is necessary to segment a region of interest of the fingerprint in order to eliminate false minutiae.

Conclusion

In this study, we prepared doped and codoped Er and Yb: YTO fluorescent powder to the aim of efficient latent fingerprint detection in crime scene. The structural and spectroscopic study of the obtained samples showed a good crystalline structure allowing high dopant concentrations, Even though the dimension of the powder grains is not nanometric, the powder showed good adhesion to the fingerprints and permitted a good visibility of the fingerprints even on smooth non-porous surfaces. Furthermore, co-doping with Yb ions permitted to suppress the $4F9/2 \rightarrow 4I15/2$ Er emission, thus eliminating the reddish halo usually present in Er-based phosphor materials. This indicates that Er,Yb:YTO phosphor grown with a simple solid-state reaction technique can be a useful fingerprint development powder thanks to its strong pure green PL signature of Er^{3+} ion. The prepared phosphor successfully developed the latent fingerprint from different surfaces in few minutes for trained investigators using the powder dusting method. This method was robust, the powders showed good adhesion with fingerprint details despite the large size of its grains and low background interference. Moreover, all the three levels of fingerprint ridge patterns were clearly visualized. The obtained results indicate that the prepared Er,Yb:YTO phosphor is suitable as fingerprint labelling agent due to its strong photoluminescence properties and can be suitable as a fingerprint developer for forensic science applications.

Author Contributions: investigation A.M., A.M., M.G., J.X. and A.T.; data analysis, M.G. and A.T.; writing—review and editing, conceptualization, methodology, supervision, project administration and funding acquisition R.M. and A.T.

Acknowledgements

We acknowledge the support from the project PBMLT from the Tunisian Ministry of Higher Education and Research and PRA_2018_34 (“ANISE”) from the University of Pisa.

Conflicts of Interest: The authors declare no conflict of interest.

References

- [1] G. S. Sodhi, J. Kaur, *Forensic. Sci. Int.* 2001, 120, 172.
- [2] R. E. Gaensslen, in *Fingerprint Technology*. CRC Press, (R.E. Gaensslen, H.C. Lee), 2001, Ch. 4.
- [3] Y. Yang, X. Liu, Y. Lu, L. Tang, J. Zhang, L. Ge, F. Li, *Anal. Methods*.2016, 8, 6293.
- [4] C. Wang, J. Zhou, L. Lulu, Q. Song, *Part. Part. Syst. Character.* 2018, 35, 1700387
- [5] B. S. Kim, Y.-J. Jin, M. A. Uddin, T. Sakaguchi, H. Y. Woo, *G. Chem. Commun.* 2015, 51, 13634.
- [6] S. Cadd, B. Li, P. Beveridge, W.T. O'Hare, A. Campbell, M. Islam, *Sci Justice*.2016, 56,247.
- [7] C.J. Shilpa, R.B. Basavaraj, G.P. Darshan, H.B. Premkumar, S.C. Sharma, H. Nagabhushana, *J. Photochem. Photobiol. A.* 2019, 376, 288.
- [8] R.B. Basavaraj, G.P. Darshan, B. Daruka Prasad, S.C. Sharma, H. Nagabhushana *J Rare Earths* 2019, 37, 32.
- [9] D. Navami, R.B. Basavaraj, S.C. Sharma, B. Daruka Prasad, H. Nagabhushana. *J. Alloys Compd.* 2018, 762, 763.
- [10] B. Marappa, M. S. Rudresha, R. B. Basavaraj, G.P. Darshan, B. Daruka Prasad, S. C. Sharma, S. Sivakumari, P. Amudha, H. Nagabhushana. *Sens. Actuator B-Chem.* 2018, 264, 426.
- [11] M. Dhanalakshmi, R.B. Basavaraj, G.P. Darshan, S.C. Sharma, H.Nagabhushana, *MICROCHEM J.* 2019,145, 226.
- [12] R. B. Basavaraj , H. Nagabhushana , G. P. Darshan , B. Daruka Prasad , M. Rahul , S. C. Sharma , R. Sudaramani , K.V. Archana . *Dyes Pigment.* 2017, 147,364.
- [13] M. Wang, *RSC Adv.* 2016, 6, 36264.
- [14] C. Xu, R. Zhou, W. He, L. Wu, P. Wu, X. Hou, *Anal Chem.* 2014, 86, 3279.
- [15] F. Gao, C. Lv, J. Han, X. Li, Q. Wang, J. Zhang, C. Chen, Q. Li, X. Sun, J. Zheng. *J. Phys. Chem. C.* 2011, 115, 21574.
- [16] W. Wang, X. Lei, Z. Ye, N. Zhao, H. Yang, *J. Alloys. Compd.* 2017, 705, 253.
- [17] S. J. Park, B. S. Je, J. W. Jang, M. Seong Oh, M. S. Koo, S. J. Yang, H. K. Yang, *J. Alloys. Compd.* 2019, 789, 367.
- [18] M. Saif. *J. Lumin.* 2013, 135, 187.
- [19] Y. -J. Kim, H. -S. Jung, J. Lim, S.-J. Ryu, and J.-K. Lee. *Langmuir*.2016, 32, 8077.
- [20] T. J. Haley, N. Komesu, G. Colvin, L. Koste, H. C. Upham. *J. Pharm Sci.*1965, 54, 643.
- [21] B. D. Hietbrink, B. E. Dubois, P. Kenneth. *Toxicol. Appl. Pharmacol.* 1963, 5, 750.
- [22] J. Wang, T. Wei, X. Li, B. Zhang, J. Wang, C. Huang, Q. Yuan. *Angew. Chem. Int. Ed.* 2014, 53, 1616.
- [23] S. Kumar, S. B. Rai, C Rath, *Part. Part. Syst. Character.* 2019, 1900048
- [24] R. Ma, R. Shimmon, A. McDonagh, P. Maynard, C. Lennard, C. Roux.*Forensic. Sci. Int.* 2012, 217, e23.13
- [25] R. Ma, E. Bullock, P. Maynard, B. Reedy, R. Shimmon, C. Lennard, C. Roux, A. M. Donagh. *Forensic Sci. Int.* 2011, 207, 145.

- [26] R. Saferstein, *Criminalistics: An Introduction to Forensic Science* Prentice Hall, New Jersey, 2006.
- [27] M. Wang, Y. Zhu, C. Mao. *Langmuir*.2015, 31, 7084.
- [28] M. Wang, M. Li, M. Yang, X. Zhang, A. Yu, Y. Zhu, P. Qiu, C. Mao *Nano. Res.* 2015, 8, 1800
- [29] S. Wilhelm. *ACS Nano*.2017, 11, 10644.
- [30] B. Z. Malkin, A. R. Zakirov, M. N. Popova, S. A. Klimin, E. P. Chukalina, E. Antic-Fidancev, Ph. Goldner, P. Aschehoug, G. Dhalenne. *Phys. Rev. B.* 2004, 70, 075112
- [31] Z. Yang, J. Zhu, D. Yan, H. Wu, R. Wang, Z. Song, X. Yu, Y. Yang, D. Zhou, Z. Yin, J. Qiu. *Opt. Mater.* 2012, 34, 1771.
- [32] Y. Guo, D. Wang, X. Zhao, F. Wang. *Mater. Res. Bull.* 2016, 73, 84.
- [33] X. Yin, H. Wang, M. Xing, Y. Fu, Y. Tian, T. Jiang, X. Luo. *J. Lumin.* 2017, 182, 183
- [34] X. Yin, H. Wang, M. Xing, Y. Fu, Y. Tian, X. Shen, W. Yu, X. Luo. *J. Rare Earths.* 2017, 35, 230.
- [35] Z. S. Chen, W. P. Gong, T. F. Chen, S. L. Li, *Bull. Mater. Sci.* 2011, 37, 429.
- [36] M. Saif, M. Shebl, A. Mbarek, A. I. Nabeel, R. Maalej, R. Shokry. *J. Photochem. Photobiol A: Chemistry.* 2015, 301, 1.
- [37] M. Saif, M. Shebl, A. Nabeel, R. Shokry, H. Hafez, A. Mbarek, K. Damak, R. Maalej, M.S.A. Abdel-Mottaleb. *Sens. Actuator B- Chem.* 2015, 220, 162.
- [38] J. Shamblin, C. L. Tracy, R.C. Ewing, F. Zhang, W. Li, C. Trautmann, M. Lang. *Acta Mater.* 2016, 117, 207.
- [39] C. J. Howard, B. A. Hunter, D. A. J. Swinkels, Rietica, *IUCR Powder Diffract.* 1997, 22, 21.
- [40] B. P. Singh, A. K. Parchur, R. S. Ningthoujam, P. V. Ramakrishna, S. Singh, P. Singh, S. B. Rai, R. Maalej. *Phys. Chem. Chem. Phys.* 2014, 16, 22665.
- [41] L. R. Haddada, I. H. Trimech, N. E. Ben Amara. A biometric watermarking approach of fingerprint images by DLDA Gabor face features without altering minutiae. In 2016 International Image Processing, Applications and Systems (IPAS) 2016, pp. 1.
- [42] L. R. Haddada, N. E. Ben Amara. *Signal Process-Image*, 2017, 55, 23.
- [43] L. R. Haddada, N. Es. Ben Amara. Biometric authentication based on multi-instance fingerprint fusion in degraded context. *International Multi-Conference on Systems, Signals and Devices (SSD)*, 2019, 21.
- [44] D. Rutovitz. *pattern recognition, J. Royal Statist. Soc*, 1966, 129, 504–530.

Table 1. Size measured of the samples

| Sample | Size measured (d.nm) | | | Mean size (d.nm) |
|------------------|-----------------------------|-----|-----|-------------------------|
| YTO :1% Yb | 543 | 514 | 552 | 536 |
| YTO :5% Yb | 423 | 311 | 416 | 383 |
| YTO :10% Yb | 486 | 425 | 499 | 470 |
| YTO :1% Er,1% Yb | 688 | 644 | 679 | 670 |
| YTO :1% Er,2% Yb | 298 | 322 | 354 | 325 |
| YTO :1% Er,3% Yb | 592 | 501 | 561 | 551 |
| YTO :12% Er | 633 | 566 | 712 | 637 |
| YTO :14% Er | 506 | 508 | 492 | 502 |
| YTO :16% Er | 467 | 427 | 480 | 458 |
| YTO :18% Er | 507 | 578 | 555 | 547 |
| YTO :20% Er | 480 | 433 | 466 | 460 |

Figure 1: XRD diffraction patterns of (a) Yb:YTO, (b) Er,Yb:YTO, (c) Er:YTO calcined at 1500°C. The bottom vertical lines indicate the positions of the theoretical pattern for pure YTO.

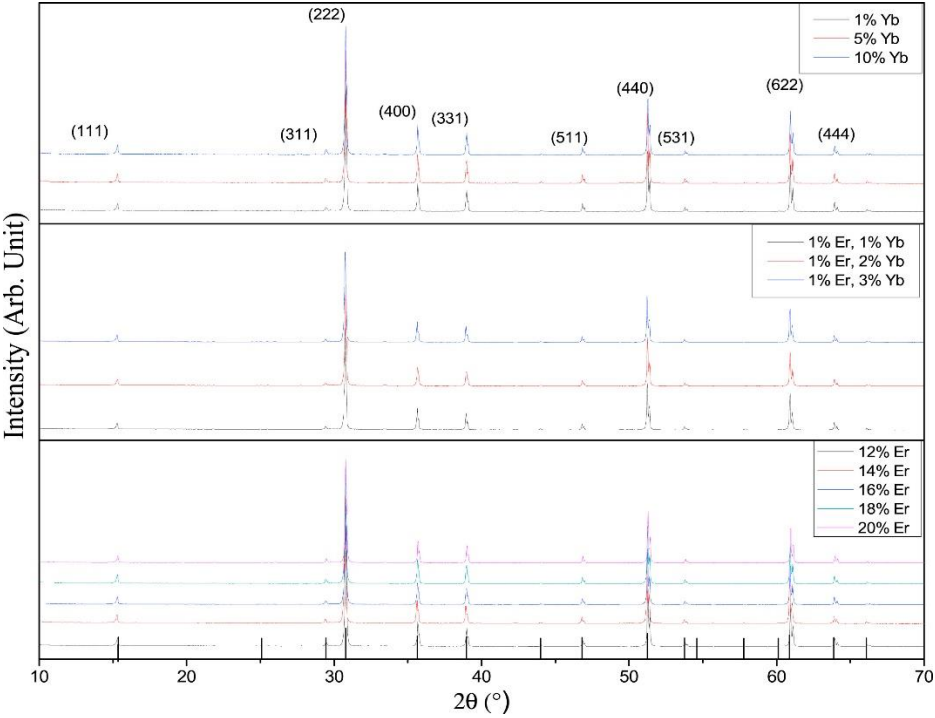


Figure 2: FTIR absorption spectra of (a) Yb:YTO, (b) Er,Yb:YTO and (c) Er:YTO

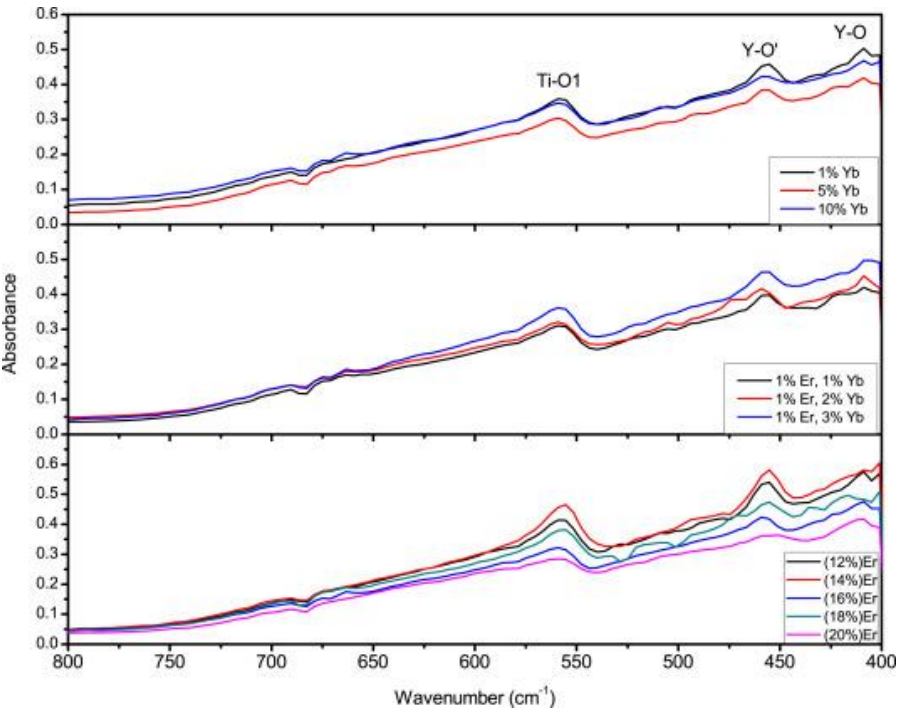


Figure 3: PL emission spectra of (a) x%Er³⁺:YTO (x=12%, 14%, 16%, 20%) (b) 1%Er³⁺+x%Yb:YTO(x=1,3%)

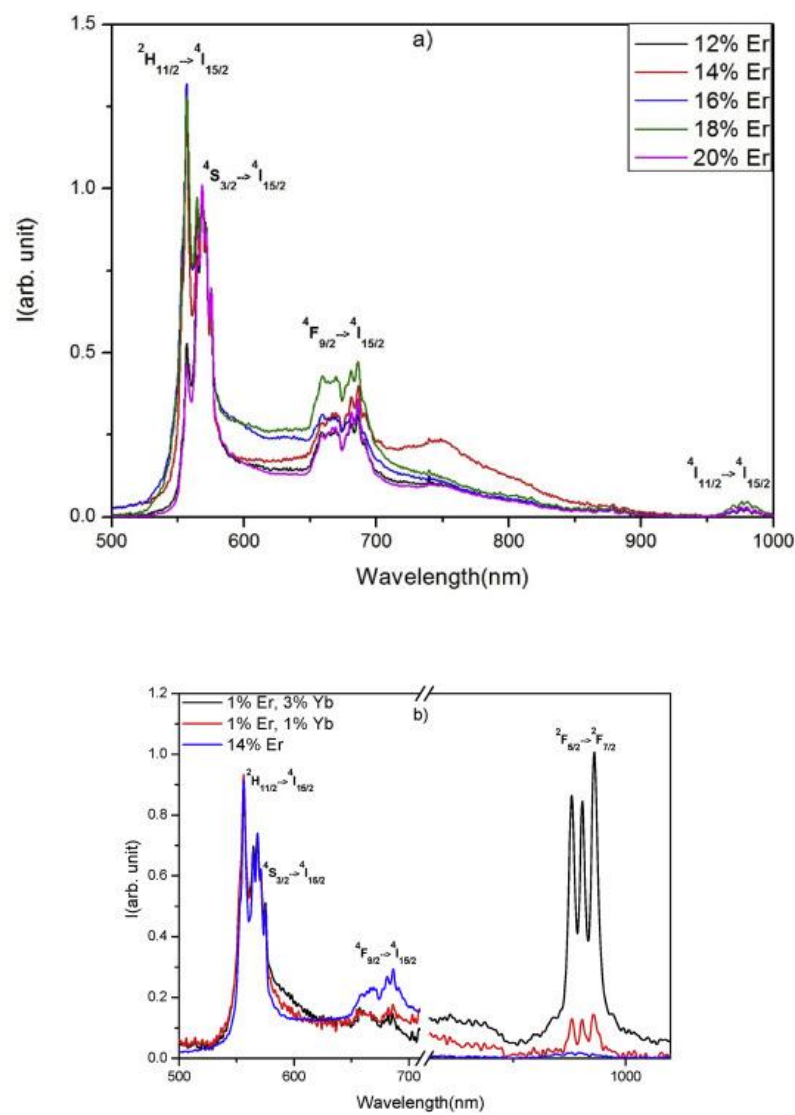


Figure 4: Illustration of the development of latent fingermarks using 1%Er, 3% Yb:YTOphosphors dusting process.

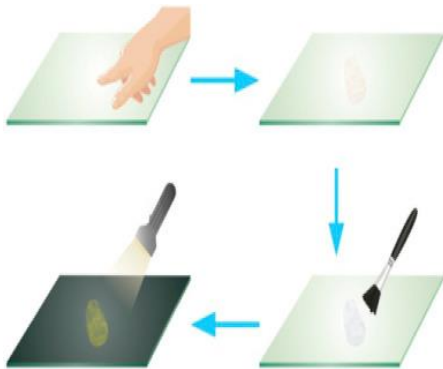


Figure 5: a-h) Latent fingermarks stained by 1%Er,3% Yb:YTOphosphors and detected on the surface of various substrates under UV or visible irradiation.

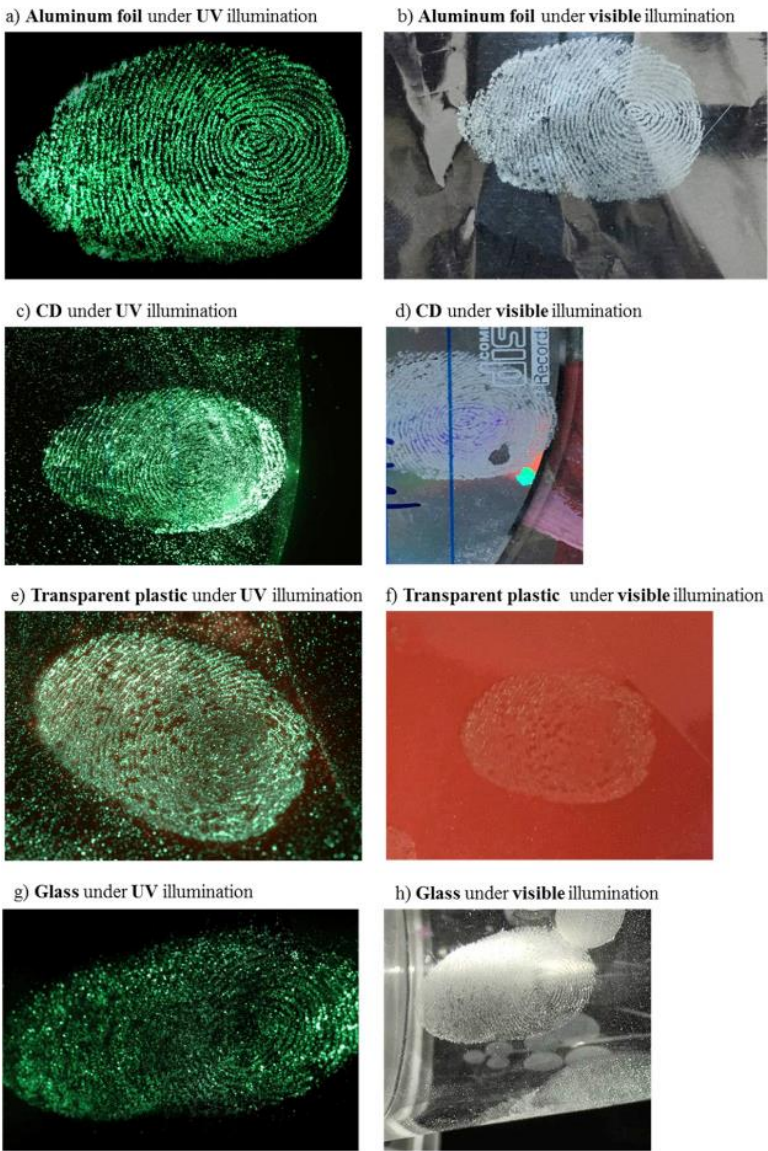


Figure 6: Ridge details evidenced by the 1%Er,3%Yb:YTO phosphors on aluminium foil under visible and UV light

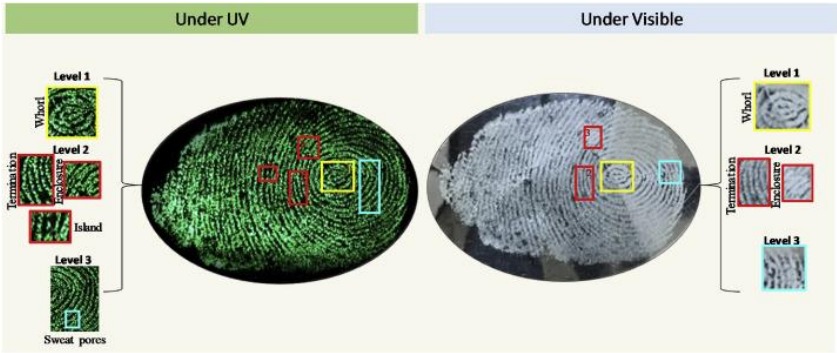


Figure 7: Minutiae extraction from latent fingerprint (a) Aluminum foil under UV illumination (b) CD under UV illumination

